A finite deformation thermomechanical constitutive model for triple shape polymeric composites based on dual thermal transitions

Qi Ge [a], Xiaofan Luo [b,c], Christian B. Iversen [b,c], Hossein Birjandi Nejad [b,c], Patrick T. Mather [b,c], Martin L. Dunn [a], H. Jerry Qi [a,*]

[a] Department of Mechanical Engineering, University of Colorado, Boulder, CO 80309, United States
[b] Syracuse Biomaterials Institute, Syracuse University, Syracuse, NY 13244, United States
[c] Department of Biomedical and Chemical Engineering, Syracuse University, Syracuse, NY 13244, United States

ABSTRACT

Shape memory polymers (SMPs) have gained strong research interests recently due to their mechanical action that exploits their capability to fix temporary shapes and recover their permanent shape in response to an environmental stimulus such as heat, electricity, irradiation, moisture or magnetic field, among others. Along with interests in conventional "dual-shape" SMPs that can recover from one temporary shape to the permanent shape, multi-shape SMPs that can fix more than one temporary shapes and recover sequentially from one temporary shape to another and eventually to the permanent shape, have started to attract increasing attention. Two approaches have been used to achieve multi-shape shape memory effects (m-SMEs). The first approach uses polymers with a wide thermal transition temperature whilst the second method employs multiple thermal transition temperatures, most notably, uses two distinct thermal transition temperatures to obtain triple-shape memory effects (t-SMEs). Recently, one of the authors' group reported a triple-shape polymeric composite (TSPC), which is composed of an amorphous SMP matrix (epoxy), providing the system the rubber-glass transition to fix one temporary shape, and an interpenetrating crystallizable fiber network (PCL) providing the system the melt-crystal transition to fix the other temporary shape. A one-dimensional (1D) material model developed by the authors revealed the underlying shape memory mechanism of shape memory behaviors due to dual thermal transitions. In this paper, a three-dimension (3D) finite deformation thermomechanical constitutive model is presented to enable the simulations of t-SME under more complicated deformation conditions. Simple experiments, such as uniaxial tensions, thermal expansions and stress relaxation tests were carried out to identify parameters used in the model. Using an implemented user material subroutine (UMAT), the constitutive model successfully reproduced different types of shape memory behaviors exhibited in experiments designed for shape memory behaviors. Stress distribution analyses were performed to analyze the stress distribution during those different shape memory behaviors. The model was also able to simulate complicated applications, such as a twisted sheet and a folded stick, to demonstrate t-SME.

© 2014 Elsevier Ltd. All rights reserved.

1. Introduction

Shape memory polymers (SMPs) are a class of smart materials capable of fixing their temporary shape and recovering to their permanent shape in response to an environmental stimulus such as heat (Lendlein and Kelch, 2002, 2005; Liu et al., 2007; Mather et al., 2009; Xie, 2011), light (Jiang et al., 2006; Koerner et al., 2004; Lendlein et al., 2005; Li et al., 2003; Long et al., 2009, 2010b, 2011; Scott et al., 2005, 2006), moisture (Huang et al.,

2005), magnetic field (Mohr et al., 2006), among others. SMPs have promising applications such as microsystem actuation components, active surface patterns, biomedical devices, aerospace deployable structures, and morphing structures. (Davis et al., 2011; Lendlein and Kelch, 2002, 2005; Liu et al., 2004, 2006; Ryu et al., 2012; Tobushi et al., 1996a; Wang et al., 2011; Yakacki et al., 2007).

For most previously developed thermally activated SMPs, a typical shape memory (SM) cycle involves two shapes: one is the permanent shape and the other one is the temporary shape (or programmed shape). This kind of SMPs is often referred to as "dual-shape" SMPs. SMPs can also be "multi-shape". There are two approaches to achieve multi-shape memory behavior. In the

first approach, the SMP has a very wide temperature range of thermal transition. Recently, Xie (2010) reported that a thermo-plastic SMP, perfluorosulphonic acid ionomer (PFSA), which has a very broad thermal transition temperature range from 55 to 130 °C, showed multi-shape SM effect if the temperature was increased in a staggered manner during free recovery. The second approach is to use multiple thermal transitions, most notably, to use two distinct transitions to obtain the triple-shape memory effects (t-SMEs). In the t-SME, the SMP is capable of fixing two temporary shapes and recovering sequentially from one temporary shape to the other, and ultimately to the permanent shape (Bellin et al., 2006, 2007; Luo and Mather, 2010; Xie et al., 2009). Several methods of achieving the t-SME were reported. For example, Bellin et al. (2006, 2007) used polymer networks consisting of two microscopic segments with two separated transitions. Xie et al. (2009) developed a macroscopic bilayer crosslinked polymer structures with two well separated phase transitions to achieve the t-SME.

Recently, based on the fabrication of shape memory elastomer composites (SMECs) (Luo and Mather, 2009), Luo and Mather (2010) introduced a new and broadly applicable method for designing and fabricating triple-shape polymeric composites (TSPCs) with well controlled properties. In the TSPC system, an amorphous SMP (epoxy with $T_g \approx 20$–40 °C, T_g, the glass transition temperature) works as a matrix providing overall elasticity and fixes one temporary shape using the glass transition; a crystallizable polymer (PCL with $T_m \sim 50$ °C, T_m, the melting temperature) interpenetrating the epoxy matrix is used as fiber network and fixes the other temporary shape using the melt-crystal transition. One advantage of this approach is its fabrication flexibility, since one can tune the functional component separately to optimize material properties (Luo and Mather, 2010). A triple-shape memory cycle of TSPC requires eight thermomechanical loading steps (Fig. 1). In Step 1 (S1), the material is deformed from L_0 to L_1 at a high temperature T_H, higher than the two thermal transition temperatures ($T_{Trans\,I}$ and $T_{Trans\,II}$). In Step 2 (S2), the temperature is cooled down to T_{L1} ($T_{Trans\,II} < T_{L1} < T_{Trans\,I}$), while maintaining the load. In Step 3 (S3), the external load is suddenly removed and the material fixes the first temporary shape (temporary shape I) at T_{L1}. In Step 4 (S4), the sample is deformed again at T_{L1}. (In practice, the loading at S4 is not necessary to have the same direction with the loading at S1.) In Step 5 (S5), the temperature is decreased to T_{L2} ($T_{L2} < T_{Trans\,II}$) while keeping the external load applied in S4. In Step 6 (S6), after a sudden removal of the external load, the second temporary shape (temporary shape II) is fixed at T_{L2}. In Step 7 (S7), once the temperature is elevated to T_{L1}, the material recovers

into its first temporary shape. In Step 8 (S8), the permanent shape is recovered by heating back to T_H.

Along with the fast development of SMPs, constitutive models also have been developed. In amorphous SMPs, where the SM effect is due to the glass transition, modeling approaches include the early model by Tobushi et al. (1996b), the continuum finite deformation thermoviscoelastic model by Nguyen et al. (2008), the finite three dimension phase based model by Qi et al. (2008), the thermo-mechanically coupled theories for large deformations of amorphous polymers by Ames et al. (2009), Anand et al. (2009), Srivastava et al. (2010a,b), the finite strain 3D thermoviscoelastic constitutive model by Diani et al. (2006), the modified standard linear solid model with Kohlrausch–Williams–Watts (KWW) stretched exponential function by Hermiller et al. (2011), and the recent three dimensional (3D) finite deformation constitutive model with a multi-branch modeling approach to represent non-equilibrium process during the glass transition by Westbrook et al. (2011a). In semicrystalline SMPs, Barot and Rao developed a constitutive model for crystallizable shape memory polymers using the notion of multiple natural configurations (Barot and Rao, 2006). Westbrook et al. successfully applied the phase-based modeling approach to the one-way and two-way SM effects in semicrystalline (Westbrook et al., 2010b). Recently, Ge et al. developed a 3D thermomechanical constitutive model for SMECs, which consists of an elastomeric matrix and crystallizable fiber networks (Ge et al., 2012). In that model, the SMEC is developed by treating matrix and fiber network as a homogenized system of multiple phases, and the fiber networks are taken to be an aggregate of melt and crystalline regions. It also gives an evolution rule for crystallization and melting from existing theories (Ge et al., 2012).

The authors have recently reported a 1D thermomechanical model to explain the underlying shape memory mechanism of t-SMP (Ge et al., 2013). In this paper, we formulate a 3D finite deformation thermomechanical constitutive model for the TSPCs. The model combines the multi-branch modeling approach for viscoelasticity of amorphous SMPs (the matrix), and the constitutive model with different deformed crystalline phases for the shape memory behavior of the crystallizable SMP (the fiber network) to describe the t-SME. For the matrix, the time–temperature superposition principle is used to describe glass transition; for the fiber network, the assumption that newly formed crystalline phases of the fiber network are initially in stress-free state is used to track the kinematics of evolving phases. The rest of the paper is arranged in the following manner: In Section 2, the material is introduced briefly and experimental results including DMA, thermomechanical
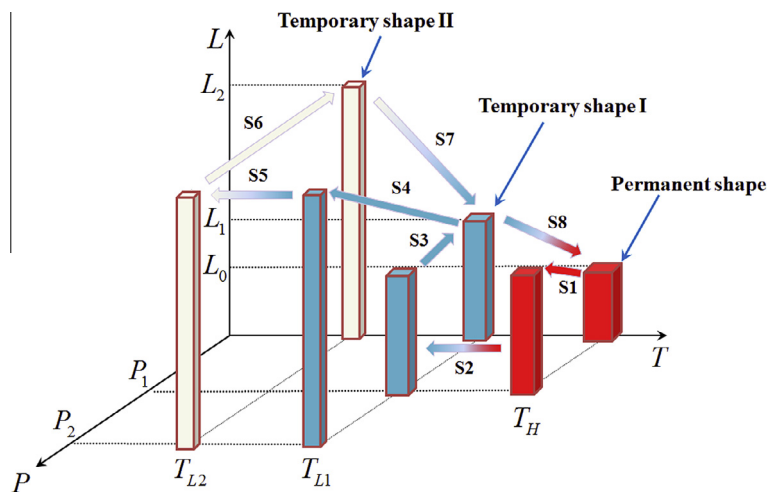

Fig. 1. Schematic of a temperature (T)-loading (P)-length (L) plot showing the eight-step thermomechanical cycle to achieve t-SME.

tests, stress relaxation tests, dual-shape and triple-shape memory behaviors are presented. Section 3 introduces a general 3D finite deformation thermomechanical constitutive model including viscoelasticity for the matrix, mechanics for the crystallizable fiber network, and the thermal expansion model. In Section 4, model simulations and predictions of shape memory behaviors are presented. Results from simulations of representative 3D problems with the user material subroutine based on this model are presented at the end.

2. Materials and thermo-mechanical behavior

2.1. Materials

The epoxy/PCL TSPC consists of an epoxy-based copolymer thermoset system as the matrix and a poly(ε-caprolactone) (PCL) as fiber reinforcements. The epoxy-based copolymer thermoset system consists of an aromatic diepoxide (diglycidyl ether of bisphenol-A or DGEBA), an aliphatic diepoxide (neopentyl glycol diglycidyl ether or NGDE) and a diamine curing agent (poly(propylene glycol) bis (2-aminopropyl) or Jaffamine D230) (Luo and Mather, 2010). The mole-% ratio DGEBA: NGDE = 30:70 or D30N70 was chosen for all tests. The fabrication was similar to previously reported shape memory elastomeric composites (SMECs) (Luo and Mather, 2009). The epoxy/PCL samples chosen in this paper for tests were made up of 82% of the epoxy-based matrix and 18% of the PCL fiber network.

2.2. DMA experiments

Dynamic Mechanical Analysis (DMA) test was conducted using a dynamic mechanical analyzer (Q800 DMA, TA Instruments). The epoxy/PCL TSPC sample (11.65 mm × 1.7 mm × 0.43 mm rectangular film) was tested using a dynamic tensile load at 1 Hz. The temperature was first decreased from 100 to −50 °C at a rate of 0.25 °C/min. After 10 min isothermal holding at −50 °C, it was heated back to 100 °C at the same rate. Fig. 2 shows the tensile storage modulus varies with the temperature. Both the heating trace and the cooling trace exhibit three storage modulus plateaus in cascade. In the heating trace, in Plateau I, the matrix (epoxy) is in the glassy state, the fiber network (PCL) is in the semicrystalline state and the storage modulus of the composite system is ~1.5 GPa. In Plateau II, where the temperature is above T_g^{epoxy} of the matrix (epoxy), the matrix transfers into the rubbery state, but the fiber network stays at the semicrystalline state. The modulus of the composite system declines into ~10 MPa. In Plateau III, where the temperature is above the T_m^{PCL} of the fiber network (PCL), the matrix stays in the rubbery state and the fiber network
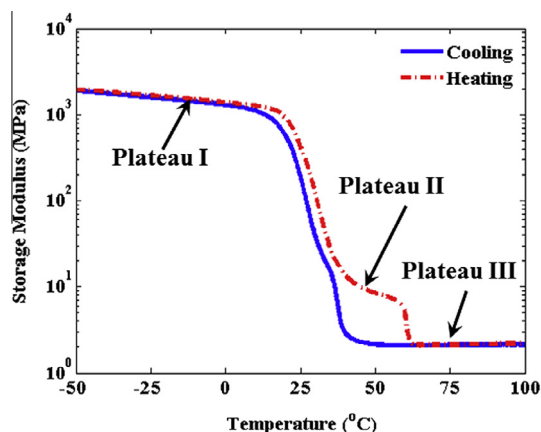

Fig. 2. The DMA test for the epoxy/PCL TSPC.

transforms from the semicrystalline state to the melt state. The storage modulus of the composite system saturates at ~2 MPa. During the cooling trace, the temperature range for Plateau II is quite narrow. We attribute this to the slow kinetics of the melt-crystal transition of the fiber network (PCL). If the cooling rate is high (>0.25 °C/min), Plateau II disappears entirely, as the rubber-glass transition of the matrix and the melt-crystal transition of the fiber network merging into a single transition step (Ge et al., 2013; Luo and Mather, 2010).

2.3. Isothermal uniaxial tension tests and thermal strain experiments

Uniaxial tension tests and thermal expansion tests for both the neat epoxy and the epoxy/PCL TSPC were conducted using the same DMA tester. Dimensions of the neat epoxy sample and the epoxy/PCL TSPC sample were 9.09 mm × 1.8 mm × 1.44 mm and 9.97 mm × 1.97 mm × 0.5 mm, respectively. The uniaxial tension tests were conducted under isothermal conditions at 40 and 80 °C, respectively. Samples were placed under isothermal conditions for a certain amount of time (30 min at 80 °C to allow melting to complete, and 60 min at 40 °C to allow crystallization to complete), and then stretched at the loading rate of 0.5 MPa/min. Fig. 3a shows the uniaxial tension results for both the neat epoxy and TSPC at 80 and 40 °C, where the strain is engineering strain and the stress is nominal stress. At 80 °C, both the epoxy and the TSPC exhibited good linearity. At 40 °C, both the epoxy and the TSPC showed slight nonlinear stress–strain behaviors. As discussed later, the uniaxial tension tests were used to identify parameters such as stress concentration factors, crosslink density of epoxy, and shear modulus of PCL crystals.

For the thermal strain experiments, samples were initially equilibrated at 100 °C for 30 min, and then cooled to −10 °C at a cooling rate of 2 °C/min. Fig 3b shows the thermal strain for both the neat epoxy and the TSPC. For the neat epoxy, above ~15 °C, the material contracts during cooling linearly with a coefficient of thermal expansion (CTE) 1.6×10^{-4}/°C; below ~15 °C, the material contracts with a lower CTE 0.6×10^{-4}/°C, as the epoxy in the glassy state. For the TSPC, above ~30 °C, the TSPC contracts linearly with a CTE 2.3×10^{-4}/°C; below ~10 °C, the TSPC contract linearly with a lower CTE 1.7×10^{-4}/°C; between 10 and 30 °C, the thermal expansion is nonlinear primarily due to melt-crystal transition of PCL. Fig 3b is used to identify parameters for the thermal strains in Section 3.4.

2.4. Stress relaxation tests

Stress relaxation tests were also conducted on the DMA tester. A rectangular TSPC sheet with dimension 8.97 mm × 1.71 mm × 0.43 mm was used for tests. Stress relaxation tests were performed at 16 different temperatures evenly distributed from 0 to 30 °C. Samples were preloaded by a 1×10^{-3} N force to maintain straightness. After reaching the testing temperature, samples were allowed 30 min for the thermal equilibration. Next, a 0.1% strain was applied to the sample within 3 s and held for 30 min. Fig. 4a shows the stress relaxation moduli under the 16 different temperatures. As expected, the relaxation moduli strongly depend on the testing temperatures. Based on the well-known time temperature superposition principle (TTSP) (Ferry, 1980; Flory, 1953), a relaxation modulus master curve at a reference temperature of 16 °C (Fig. 4b) was constructed by shifting relaxation curves using shift factors at different temperatures (Fig. 4c).

2.5. Triple-shape memory behavior

The triple shape memory behavior test was conducted using the DMA machine by following the eight-step thermomechanical cycle introduced in Section 1 with a 10.69 mm × 2.25 mm × 0.42 mm
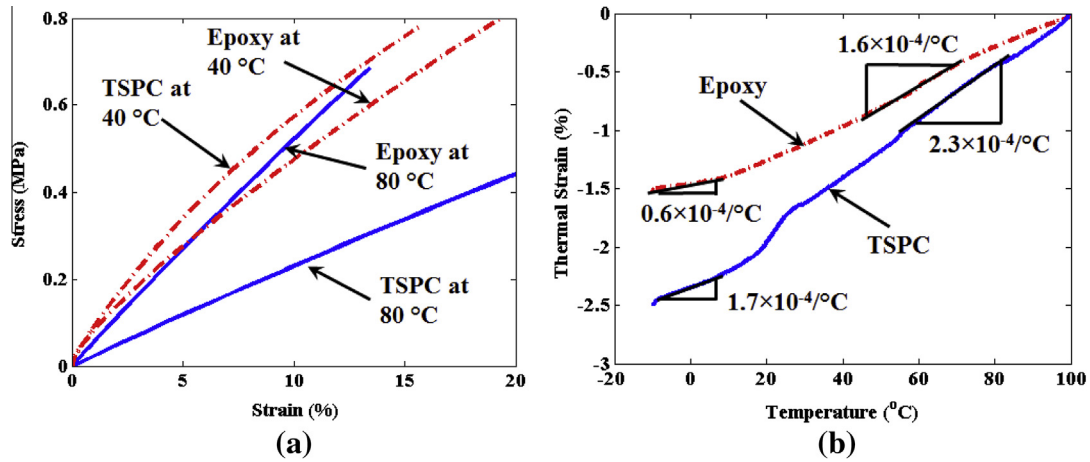
Fig. 3. Thermal and mechanical tests for the neat epoxy and the TSPC: (a) the uniaxial tensions; (b) the thermal strains for the neat epoxy and TSPC.
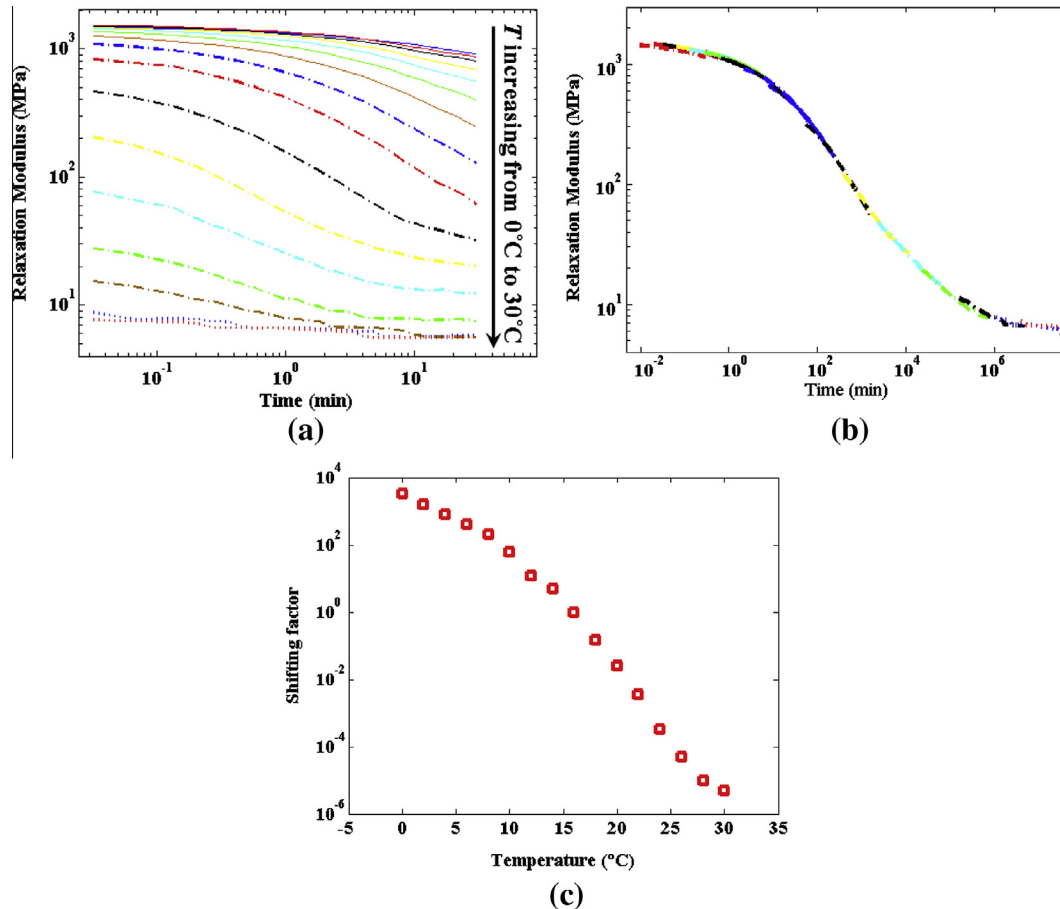

Fig. 4. Stress relaxation tests: (a) stress relaxation moduli vs. time under 16 temperatures varying from 0 to 30 °C with 2 °C interval; (b) the stress relaxation modulus master curve at 16 °C; (c) the shifting factors at the 16 temperatures for achieving the master curve.

epoxy/PCL TSPC rectangular film: in step S1, the material was stretched by a nominal stress P_1 at T_H, (P_1 is 0.15 MPa ramped with a loading rate of 0.5 MPa/min in Fig. 5). In S2, the material was cooled down to a temperature T_{L1} (T_{L1} is 40 °C in Fig. 5) at a rate of 2 °C/min, while maintaining P_1. After arriving at T_{L1}, it was iso-thermally held for 1 h to make sure the crystallization of PCL com-plete. In S3, the external load was removed and the first temporary shape was achieved. In S4, the material was stretched again by a nominal stress P_2 (P_2 is 0.45 MPa ramped with a rate of 0.5 MPa/min to in Fig. 5) at T_{L1}. In S5, it was cooled down to T_{L2} (T_{L2} is 0 °C

in Fig. 5) at the same cooling rate with S2, while keeping P_2. In S6, P_2 was removed and the second temporary shape was fixed. In S7, by heating back to T_{L1} at a rate of 2 °C/min, the sample precisely recovered to its first temporary shape. In S8, the sample completely recovered to the permanent shape by heating back to T_H.

2.6. One-step-fixing shape memory behavior

The epoxy/PCL TSPC is also capable of exhibiting the so called "one-step-fixing shape memory behavior" (Ge et al., 2013; Luo
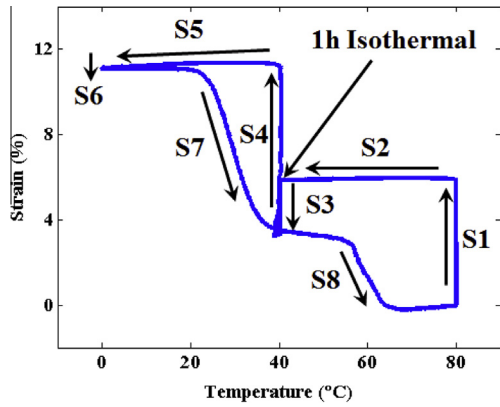
Fig. 5. The strain-temperature plot for the triple shape memory behavior of the epoxy/PCL TSPC.

and Mather, 2010). Fig. 6 shows the strain-temperature plot of this one-step-fixing shape memory behavior: at T_H (T_H is 80 °C in Fig. 6), the sample was stretched under a nominal stress P (P is 0.2 MPa ramped with a loading rate of 0.5 MPa/min). Then, it was cooled down to a low temperature T_L (0 °C) at a rate of 2 °C/min, while the load P was maintained as constant. After the removal of P, the temporary shape was fixed at T_L. During heating from T_L to T_H at a rate of 2 °C/min, a strain plateau from ~30 to 55 °C was observed and part of the strain (~60%) was still fixed at this plateau. Raising the temperature further, the recovery resumed at ~55 °C and the sample returned to its permanent shape at ~65 °C.

3. Model description

3.1. Overall model

In this section, a 3D finite deformation thermomechanical constitutive framework for TSPCs is developed by treating matrix and the fiber network as a homogenized system of multiple phases. The matrix is taken as an amorphous SMP and the fiber network is taken to be an aggregate of melt and crystalline regions. The goal is to develop a modeling approach for this class of materials. At this point, some levels of detailed understanding are sacrificed in favor of a simple way to describe the complex thermo-mechanical phenomena and therefore several assumptions are made:

(a) For the sake of simplicity, the framework adopts neo-Hookean model to describe the stress–strain behavior of the equilibrium branch of the matrix and the crystalline phase of the
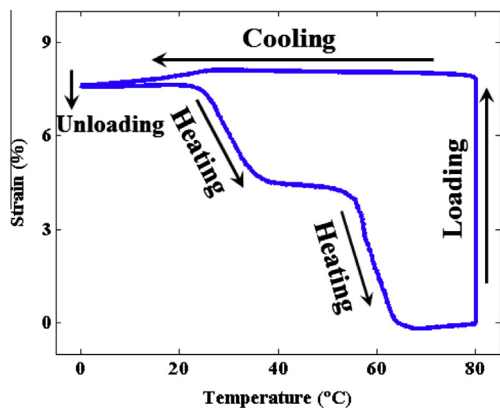

Fig. 6. The strain-temperature plot for one-step-fixing shape memory behavior of the epoxy/PCL TSPC.

fiber network. A more sophisticated model can be used to replace neo-Hookean under large deformations. (Arruda and Boyce, 1993; Gent, 1996; Mooney, 1940; Rivlin, 1948).

(b) As the specimens are thin (<0.5 mm), the heat conduction effect is ignored in the current framework. If considering a general case, the heat conduction effect can be included and the heat conduction related parameters can be easily measured (Westbrook et al., 2010a, 2011a).

(c) In the crystallizable fiber network, it is assumed that the fiber does not carry load at temperatures above the melting temperature. During crystallization, crystalline phases are formed in a stress-free (natural) configuration (Rajagopal and Srinivasa, 1998a,b). The crystalline phases formed at different times have different deformation history.

(d) In the current framework, the modified Avrami's theory (Avrami, 1939, 1940, 1941; Ozawa, 1971) was used to describe the crystallinity during the isothermal crystallization. In a general case, the Evans theory and Hoffman–Lauritze expression can be used to describe the non-isothermal crystallization. (Ge et al., 2012)

Here, we consider a 3D solid body in its initial configuration Ω_0 deforms into the current configuration, Ω. Following continuum mechanics, we consider a material point containing numerous material particles, which consist of the amorphous SMP matrix with a volume fraction of v_M and the crystallizable fiber network with a volume fraction of v_F. At time $t = 0$, a material point in Ω_0 occupies point **X** at the temperature T_0. $\mathbf{x}(\mathbf{X}, t = n\Delta t)$ gives the current position of the material point **X** at time $t = n\Delta t$, in Ω, and the temperature changes to T_n. The deformation gradient is defined by $\mathbf{F} = \partial \mathbf{x}/\partial \mathbf{X}$.

Fig. 7 shows the one dimensional (1D) arrangement of rheological elements in the model, which decomposes the total deformation gradient $\mathbf{F}_{total}$ into the mechanical deformation gradient $\mathbf{F}_M$ and the thermal deformation gradient $\mathbf{F}_T$:

$$\mathbf{F}_{total} = \mathbf{F}_M \mathbf{F}_T. \tag{1}$$

For the mechanical elements, the left set of spring-dashpot branches represents the stress acting on the amorphous SMP matrix; the right set of branches represents the stress acting on the crystallizable fiber network. The total Cauchy stress on the TSPC system is given by:

$$\boldsymbol{\sigma}_{total} = \gamma_M v_M \boldsymbol{\sigma}_M + \gamma_F v_F \boldsymbol{\sigma}_F, \tag{2}$$

where $\boldsymbol{\sigma}_M$ and $\boldsymbol{\sigma}_F$ are the stresses acting on the matrix and the fiber network. Here, the concept of the stress concentration factors from the micromechanics of heterogeneous solids in linear and nonlinear elasticity (Benveniste, 1987; Castaneda, 1991; Dunn, 1997) are adopted to take into account the stress distribution on the phases, which is highly dependent on details of the microstructure, such as the geometry, and architecture of the spatial arrangement of the phases, and the evolution of their properties. γ_M and γ_F are the stress concentration factors of the matrix and the fiber network, and $\gamma_M v_M + \gamma_F v_F = 1$. For the sake of brevity, we denote $\gamma_M v_M$ and $\gamma_F v_F$ as $\bar{v}_M$ and $\bar{v}_F$.

3.2. Viscoelastic behavior of the matrix

In Fig. 7, an equilibrium branch and several nonequilibrium branches are arranged in parallel. Each nonequilibrium branch is a nonlinear Maxwell element where an elastic spring and a dashpot are placed in series. The set of nonequilibrium branches represents different modes of the relaxation behavior, which are either structural or segmental relaxation of polymers. The total Cauchy stress acting on the matrix $\boldsymbol{\sigma}_M$ is:
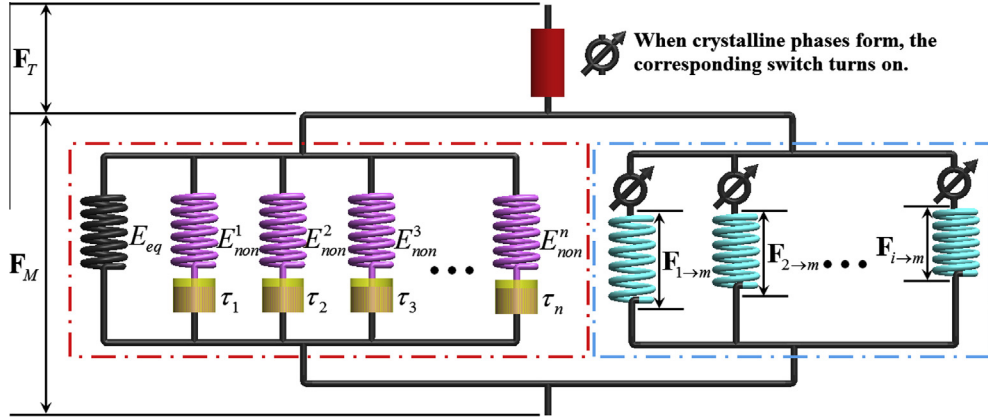
Fig. 7. The 1D rheological schematic of the proposed model: the total deformation gradient $\mathbf{F}_{total}$ can be decomposed into the mechanical deformation gradient $\mathbf{F}_M$ and the thermal deformation gradient $\mathbf{F}_T$. The total Cauchy stress consists of the stress on the matrix (the left red box) and the stress on the fiber network (the right blue box). (For interpretation of the references to color in this figure legend, the reader is referred to the web version of this article.)

$$\boldsymbol{\sigma}_M = \boldsymbol{\sigma}_{eq} + \sum_{i=1}^{n} \boldsymbol{\sigma}_{non}^i, \tag{3}$$

where $\boldsymbol{\sigma}_{eq}$ and $\boldsymbol{\sigma}_{non}^i$ are Cauchy stresses in equilibrium branch and the ith nonequilibrium branch, respectively.

3.2.1. Hyperelastic behavior of the equilibrium branch

Hyperelastic material models typically for rubbers are used for the equilibrium behaviors. Here, the neo-Hookean model is adopted to define $\boldsymbol{\sigma}_{eq}$:

$$\boldsymbol{\sigma}_{eq} = \frac{Nk_BT}{J_M}\left(\bar{\mathbf{B}} - \frac{1}{3}\mathrm{tr}\bar{\mathbf{B}}\right) + K_{eq}(J_M - 1)\mathbf{I}, \tag{4}$$

where N is the crosslinking density, k_B is Boltzmann's constant, T is the absolute temperature. Nk_BT is the temperature dependent shear modulus, which indicates entropic elasticity. K_{eq} is the bulk modulus of the equilibrium branch, which is typically orders of magnitude larger than the shear modulus. $\bar{\mathbf{B}}$ is the modified left Cauchy–Green tensor given by $\bar{\mathbf{B}} = \bar{\mathbf{F}}_M(\bar{\mathbf{F}}_M)^T$, with $\bar{\mathbf{F}}_M = (J_M)^{-1/3}\mathbf{F}_M$ and $J_M = \det(\mathbf{F}_M)$.

3.2.2. Viscoelastic behavior of nonequilibrium branches

For the nonequilibrium behaviors in the ith viscoelastic branches, the deformation gradient can be further decomposed into an elastic part and a viscous part:

$$\mathbf{F}_M = \mathbf{F}_e^i \mathbf{F}_v^i, \tag{5}$$

where $\mathbf{F}_v^i$ is a relaxed configuration obtained by elastically unloading by $\mathbf{F}_e^i$. The Cauchy stress on ith nonequilibrium branch, $\boldsymbol{\sigma}_{non}^i$, is given by:

$$\boldsymbol{\sigma}_{non}^i = \frac{1}{J_e^i}(\mathbf{L}_e^i : \ln \mathbf{V}_e^i), \tag{6}$$

where $J_e^i = \det(\mathbf{F}_e^i)$, $\mathbf{V}_e^i = \mathbf{F}_e^i(\mathbf{R}_e^i)^T$ and $\mathbf{R}_e^i$ is the rotation tensor. $\mathbf{L}_e^i$ is the fourth order isotropic elasticity tensor which is taken by:

$$\mathbf{L}_e^i = 2\mu_i\left(I - \frac{1}{3}\mathbf{I}\otimes\mathbf{I}\right) + 2K_i\mathbf{I}\otimes\mathbf{I}, \tag{7}$$

where I is the fourth order identity tensor, μ_i and K_i are shear and bulk moduli for the ith branch, respectively. In the above equations, the symbol (:) represents a tenor double contraction and ($\otimes$) represents the tensor dyadic product; μ_i is the shear modulus; K_i is typically orders of magnitude larger than the shear modulus.

In each nonequilibrium branch, the second Piola–Kirchoff stress in the intermediate configuration (or elastically unload configuration) and the Mandel stress are given by:

$$\mathbf{S}_{non}^i = J_e^i(\mathbf{F}_e^i)^{-1}\boldsymbol{\sigma}_{non}^i(\mathbf{F}_e^i)^{-T} \quad \text{and} \quad \mathbf{M}_{non}^i = \mathbf{C}_e^i\mathbf{S}_{non}^i, \tag{8}$$

where $\mathbf{C}_e^i = (\mathbf{F}_e^i)^T\mathbf{F}_e^i$ is the right Cauchy–Green deformation tensor. Typically for inelastic materials, the Mandel stress is used to drive the viscous flow $\dot{\gamma}_v^i$ via the equivalent shear stress:

$$\dot{\gamma}_v^i = \frac{\bar{M}_i}{\mu_i\tau_i(T)}, \tag{9}$$

where the temperature dependent relaxation time $\tau_i(T)$ will be discussed in the next section and the equivalent shear stress is defined as $\bar{M}_i = [\frac{1}{2}(\mathbf{M}_i)' : (\mathbf{M}_i)']^{1/2}$ with $(\mathbf{M}_i)' = \mathbf{M}_i - 1/3\mathrm{tr}(\mathbf{C}_e^i)\mathbf{I}$.

The viscous stretch rate $\mathbf{D}_v^i$ is constitutively prescribed to be:

$$\mathbf{D}_v^i = \frac{\dot{\gamma}_v^i}{\sqrt{2}\bar{M}_i}\mathbf{M}_i. \tag{10}$$

As discussed previously in Boyce et al. (1988), $\mathbf{D}_v^i$ can be made equal to the viscous spatial velocity gradient $l_v^i = \dot{\mathbf{F}}_v^i(\mathbf{F}_v^i)^{-1}$ by ignoring the spin rate $\mathbf{W}_v^i$ and therefore:

$$\dot{\mathbf{F}}_v^i = \mathbf{D}_v^i\mathbf{F}_v^i. \tag{11}$$

3.2.3. Temperature dependent relaxation time

The relaxation times of each nonequilibrium branch are temperature dependent, with the temperature dependent stress relaxation time $\tau_i(T)$ being obtained from the reference time using a shifting factor a_T:

$$\tau_i(T) = a_T\tau_{0i}, \tag{12}$$

where τ_{0i} is the stress relaxation time at a reference temperature. It was found that depending on whether temperature is above, near, or below T_g, the shifting factor a_T can be calculated by two different method (O'Connell and McKenna, 1999):

$$a_T = \begin{cases} 10^{-\frac{C_1(T-T_r)}{C_2+(T-T_r)}} & T \geqslant T_r \\ e^{-\frac{AF_C}{k}\left(\frac{1}{T}-\frac{1}{T_r}\right)} & T < T_r \end{cases}, \tag{13}$$

where C_1, C_2 and A are material constants, F_c is the configuration energy, k is Boltzmann's constant and T_r is the reference temperature. Parameters in Eqs. (12) and (13) can be identified by stress relaxation tests and will be discussed in Section 4.1.2.

3.3. Mechanical behavior of the crystallizable fiber network

In Fig. 7, a set of springs is used to represent the mechanical behavior of the crystallizable fiber network. During crystallization, fiber crystals form gradually. Once a small piece of crystalline

phase forms, the corresponding switch in Fig. 7 turns on. More specifically, we assume that crystals are formed in a stress-free (natural) configuration. Upon such incremental crystallization, the entire material may undergo an immediate deformation. Thus, we further assume that the deformation transfer can be simplified by an averaging scheme that assumes both the matrix and fiber crystals undergo a small deformation increment. These assumptions were used to model different active polymer systems (Ge et al., 2012; Long et al., 2009, 2010a,b, 2011, 2013; Ryu et al., 2012; Westbrook et al., 2011b) in the past. Depending on the thermomechanical condition, the crystalline phases forming at different times may have different deformation histories. During melting, the crystalline phases melt gradually. In terms of the kinetics of the melting process, the portions of crystalline phases that form at a later time melt first (Ge et al., 2012). Once a small portion of crystalline phases melts, the corresponding switch in Fig. 7 turns off and does not carry any load.

3.3.1. Constitutive model for crystalline phases

For the convenience of model description, we assume fiber crystals also follow the hyperelastic behavior and the neo-Hookean model is used to describe the Cauchy stress on fiber crystals:

$$\boldsymbol{\sigma}_F^C(\mathbf{F}) = \frac{\mu_C}{J}\left(\bar{\mathbf{B}} - \frac{1}{3}\text{tr}\bar{\mathbf{B}}\right) + K_C(J-1)\mathbf{I}, \tag{14}$$

where $\mathbf{F}$ is the deformation gradient μ_C and K_C are shear and bulk moduli for fiber crystals.

3.3.2. Mechanics during crystallization

As indicated above, during crystallization, we assume that when a small portion of crystalline phase forms, it is in a stress-free state. In order to satisfy boundary conditions, either overall or locally, however, this small piece of crystalline phase will deform immediately. This stress-free state for newly forming crystalline phases was referred to as the natural configuration by Rajagopal and Srinivasa (1998a,b). According to the algorithm for SMEC (Ge et al., 2012), for a crystalline phase forming at time $t = t_0 + i\Delta t$, its deformation gradient at the current time $t = t_0 + m\Delta t$ $(m > i)$ is the accumulative deformation gradient from $t = t_0 + i\Delta t$ to $t = t_0 + m\Delta t$, $\mathbf{F}_{i\rightarrow m}$:

$$\mathbf{F}_{i\rightarrow m} = \prod_{j=i}^{m}{}^{L}\Delta\mathbf{F}_j = \mathbf{F}_m(\mathbf{F}_i)^{-1}, \tag{15}$$

where $\prod_{i=1}^{n}{}^{L}()_i = ()_n \cdots ()_2()_1$. $\Delta\mathbf{F}_j$ is the incremental deformation gradient at $t = t_0 + j\Delta t$.

The total Cauchy stress on the crystallizable fiber network equals to the summation of individual crystalline phase forming at different time weighted by its own volume fraction:

$$\boldsymbol{\sigma}_F = \sum_{i=1}^{m}[\Delta v_i^C \boldsymbol{\sigma}_F^C(\mathbf{F}_{i\rightarrow m})], \tag{16}$$

where Δv_i^C is the volume fraction of the crystalline phase formed at time $t = t_0 + i\Delta t$ and the calculation of Δv_i^C will be discussed in next section.

For deformation gradients within crystalline phases during melting, it is essentially a reverse process of crystallization. Assuming that at the starting point of the melting process time $t = t_{ml}$, the total number of crystalline phases (which is equal to the total number of time increments during crystallization) is m_e. Recalling that crystalline phases that form later melt earlier, the crystalline phases melt gradually from the m_e-th phase to the 1st phase. For instance, at time $t = t_{ml} + \Delta t$, the m_e-th crystalline phase melts with its volume fraction $\Delta v_{m_e}^c$, and at time $t = t_{ml} + m\Delta t$, the $(m_e - m + 1)$-th crystalline phase melts with its volume fraction

$\Delta v_{m_e-m+1}^c$. Concurrently to the melting process, for example, at time $t = t_{ml} + m\Delta t$, a small deformation $\Delta\mathbf{F}_m^{melt}$ is induced. Following the same assumption for the mechanical deformation during crystallization, we assume that the deformation $\Delta\mathbf{F}_m^{melt}$ is applied to all the existing crystalline phases from the 1st to the $(m_e - m)$-th. Therefore, the total stress is

$$\boldsymbol{\sigma}_F = \sum_{i=1}^{m_e-m}\left[\Delta v_i^C \boldsymbol{\sigma}_F^C\left(\mathbf{F}_{1\rightarrow m}^{melt}\mathbf{F}_{i\rightarrow ml}\right)\right],$$
$$\mathbf{F}_{1\rightarrow m}^{melt} = \prod_{i=1}^{m}{}^{L}\Delta\mathbf{F}_i^{melt}. \tag{17}$$

Details about the mechanics during melting were discussed in Ge et al. (2012). In addition, the effective phase model (EPM) (Long et al., 2010a) for the phase evolution of crystalline phases is adopted to enhance computational efficiency, when implementing the constitutive model into finite element analysis. Details about the algorithm for combining crystalline phases formed at different times into one effective phase were presented in Ge et al. (2012).

3.3.3. Kinetics of crystallization and melting

The modified Avrami's theory (Avrami, 1939, 1940, 1941; Ozawa, 1971) was use to describe the crystallinity during the isothermal crystallization. At time $t = t_0 + i\Delta t$:

$$v_i^C = v_\infty\{1 - \exp[-k \cdot (t)^n]\}, \tag{18}$$

where k is a constant related the growth rate of crystallization, n is a constant related to the dimension of the crystals, and v_∞ is the saturated crystallinity at certain condition. For the PCL network, v_∞ is taken to be 25% (Ge et al., 2012). The increment of crystallinity or the volume fraction of crystalline phase form at time $t = t_0 + i\Delta t$, Δv_i^C, is:

$$\Delta v_i^C = v_i^C - v_{i-1}^C. \tag{19}$$

Δv_i^C is used in Eq. (16) to calculate the total Cauchy stress on the crystallizable fiber network.

3.4. Thermal expansion

The thermal expansion is assumed to be isotropic, i.e.,

$$\mathbf{F}_T = J_T\mathbf{I}, \tag{20}$$

where J_T is the volume change due to thermal expansion, i.e.,:

$$J_T = \frac{V(T)}{V_0}, \tag{21}$$

where $V(T, t)$ is the instantaneous volume at temperature T, V_0 is the reference volume at the reference temperature T_0. It is well known that as amorphous polymers vitrify, they transfer from an equilibrium rubbery state to a nonequilibrium glassy state. During the transition, the volume change is a function both of temperature and time. In addition, if the temperature is far below T_g, the dependence on time can become very weak (as the time constant for this dependence can be very long) (Hutchinson, 1995; McKenna, 1989). In the past, different theories (Kovacs et al., 1979; Moynihan et al., 1976; Robertson et al., 1984) have been developed to represent the evolution of the nonequilibrium volume change. The nonlinear volume change can also be simplified by a bilinear representation,

$$dV(T) = 3\alpha_r dT, (T > T_g) \quad \text{and} \quad dV(T) = 3\alpha_g dT, (T \leqslant T_g), \tag{22}$$

where α_r and α_g for the coefficients of thermal expansion (CTE) of the rubbery state and the glassy state, respectively. The instantaneous volume at temperature T is the integral of the volume change:
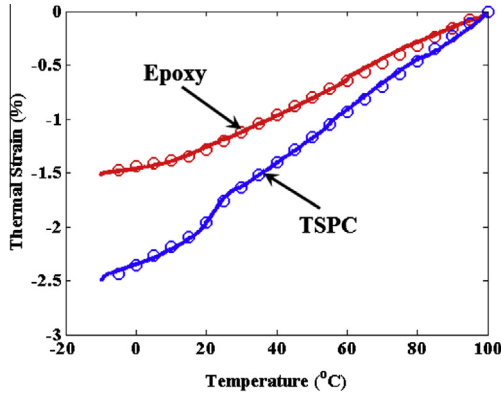
Fig. 8. Model predictions for thermal expansion of the neat epoxy and the TSPC. (Solid lines represent experiments and circles represent model predictions).

Fig. 9. Model fitting for uniaxial loading. (Continuous lines represent experiments and discrete circles represent model fittings).

$$V(T) = \int_{T_0}^{T} dV(T), \tag{23}$$

In Fig. 8, the model with $\alpha_r = 1.6 \times 10^{-4}/°C$ and $\alpha_g = 0.6 \times 10^{-4}/°C$ measured from Fig. 3b predicts the thermal expansion of the neat epoxy. T_g in Eq. (22) equals to T_r in Eq. (13), which is determined by stress relaxation tests.

TSPC at high temperatures ($T > T_m > T_g$) expands/contracts linearly with a high CTE, and the instantaneous volume change is:

$$dV(T) = 3\alpha_1^{TSPC}dT, (T > T_m > T_g), \tag{24}$$

where $\alpha_1^{TSPC} = 2.3 \times 10^{-4}/°C$ measured from Fig. 3b. We can also express α_1^{TSPC} as $\alpha_1^{TSPC} = \bar{v}_M\alpha_r + \bar{v}_F\alpha_m$, where α_m is the CTE of PCL melts and $\alpha_m = 3 \times 10^{-4}/°C$. At low temperatures ($T \leqslant T_g$), the TSPC contracts linearly with a low CTE, and the instantaneous volume change is:

$$dV(T) = 3\alpha_2^{TSPC}dT, (T \leqslant T_g), \tag{25}$$

where $\alpha_2^{TSPC} = 1.7 \times 10^{-4}/°C$ measured Fig. 3b. Here, α_2^{TSPC} can also be expressed as $\alpha_1^{TSPC} = \bar{v}_M\alpha_g + \bar{v}_F[(1 - v_\infty)\alpha_m + v_\infty\alpha_c]$, where α_c is the CTE of PCL crystals and $\alpha_c = 1.8 \times 10^{-4}/°C$. At temperatures between T_m and T_g, a volume shrink due to the melt-crystal transition of PCL is observed, and the instantaneous volume change is:

$$dV(T) = 3\alpha_3^{TSPC}(T)dT + V_S dv^C(T), \ (T_g < T < T_m), \tag{26}$$

where $\alpha_3^{TSPC}(T) = \bar{v}_M\alpha_r + \bar{v}_F\{[1 - v^C(T)]\alpha_c + v^C(T)\alpha_c\}$, and V_S is the volume shrink when PCL is 100% crystallized and it is 2.7×10^{-2}. Fig. 8 shows the model fitting for the thermal expansion of the epoxy/PCL TSPC.

4. Results

4.1. Parameter identification

4.1.1. Uniaxial tensions

Experimental results for the neat epoxy and the epoxy/PCL TSPC introduced in Section 2 were used to identify parameters for the model. The uniaxial tension tests at 80 °C (Fig. 9) were used to determine the crosslinking density N for the epoxy matrix and stress concentration factors γ_M and γ_F. As the neat epoxy is in the rubbery state at 80 °C, the relaxation time is faster than the loading rate and only the equilibrium branch carries load. For the uniaxial tension, we assume $K_{eq} = 1$ GPa (three orders of magnitude larger than the shear modulus), to ensure the material incompressibility. Consequently, Eq. (4) reduces into a 1D form:

$$\sigma_{eq} = \frac{2Nk_BT}{3}\left(\lambda^2 - \frac{1}{\lambda}\right), \tag{27}$$

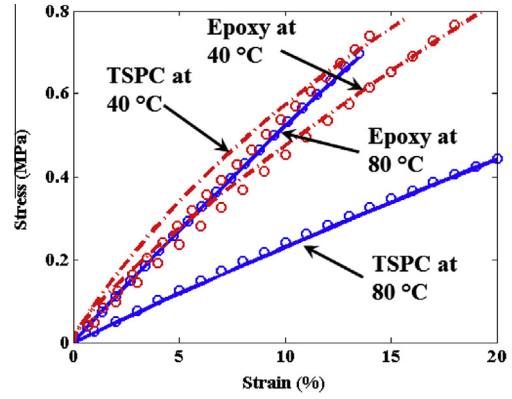where the material stretch $\lambda = L/L_0$, L and L_0 are the current and the initial length, respectively. N is identified as 5.76×10^{23} m^{-3}. For the epoxy/PCL TSPC, PCL fibers are in melt state at 80 °C and the total Cauchy stress on the TSPC is $\sigma_{total} = \gamma_M v_M\sigma_{eq}$. The total Cauchy stress in 1D form is:

$$\sigma_{total} = v_M\gamma_M\frac{2Nk_BT}{3}\left(\lambda^2 - \frac{1}{\lambda}\right). \tag{28}$$

By fitting the uniaxial tension for the TSPC at 80 °C (Fig. 9), $\gamma_M = 0.57$ and $\gamma_F = 2.94$, as $v_M = 0.82$, $v_F = 0.18$, and $\gamma_M v_M + \gamma_F v_F = 1$.

For neat epoxy, the model predicts the experimental observations well and the modulus decreases at 40 °C to the value determined by entropic elasticity. For the TSPC at 40 °C, PCL crystallizes with crystallinity v_∞ and the Cauchy stress in 1D form follows:

$$\sigma_{total} = \gamma_M v_M\frac{2nk_BT}{3}\left(\lambda^2 - \frac{1}{\lambda}\right) + \gamma_F v_F v_\infty\frac{2\mu_C}{3}\left(\lambda^2 - \frac{1}{\lambda}\right). \tag{29}$$

In Eq. (29), μ_C can be identified by fitting the uniaxial tension for TSPC at 40 °C and $\mu_C = 13.8$ MPa.

4.1.2. Stress relaxation

Stress relaxation tests were used to identify parameters of nonequilibrium branches. The stress relaxation master curve at 16 °C can be described by Maxwell elements in parallel and the stress relaxation modulus is:

$$E(t) = E_\infty + \sum_{i=1}^{n}E_i\exp\left[-\left(\frac{t}{\tau_{0i}}\right)\right]$$
$$\text{with} \quad \tau_{0i} = 10^{i-1}\tau_{01}, (i = 2,\ldots,n), \tag{30}$$

In Eq. (30), E_∞ is the relaxation modulus at time $t = \infty$ ($E_\infty = 7$ MPa in Fig. 4b); E_i and τ_{0i} are modulus and relaxation time for the i-th branch at the reference temperature (16 °C), respectively. We assume that the relaxation time of the i-th branch is a decade longer than the $(i - 1)$-th branch. At time $t = 0$, the relaxation modulus of the TSPC system is $E(0) = E_\infty + \sum_{i=1}^{n}E_i$.

Fig. 10 presents the model fitting for the stress relaxation. In Fig. 10a, one nonequilibrium branch ($n = 1$) was used to describe the stress relaxation modulus master curve. Based on Eq. (30) ($E(0) = E_\infty + E_1$), one has $E_1 = 1422$ MPa ($E(0) = 1429$ MPa and $E_\infty = 7$ MPa in Fig. 10a). Through the observation of the stress relaxation master curve in Fig. 10a, the obvious stress relaxation occurs at ~5 min. Here, $\tau_{01} = 180$ s was taken for the relaxation time of the first nonequilibrium branch. It is shown that that increasing number of nonequilibrium branches is required to precisely describe the stress relaxation modulus master curve. Fig. 10b and c shows
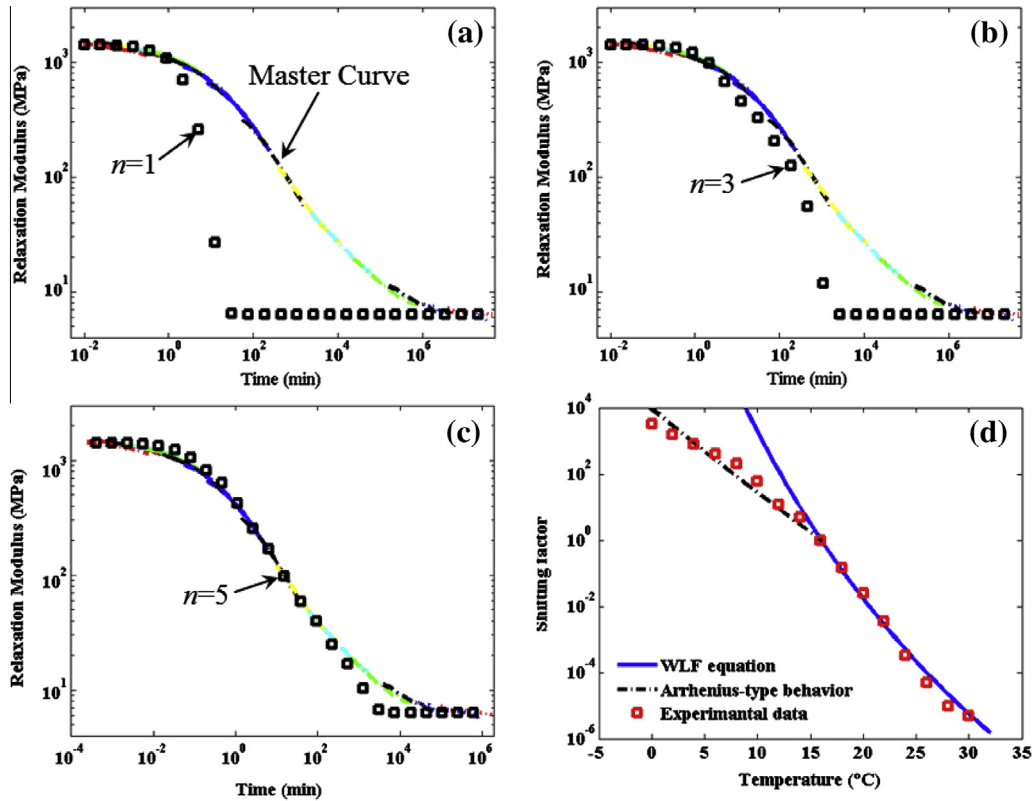
Fig. 10. Model fitting for stress relaxation: (a)–(c) the stress relaxation master curve at 16 °C; (d) the shifting factors with temperature.

the model fitting for the stress relaxation with $n = 3, 5$ nonequilibrium branches and the model fitting improves dramatically by introducing more nonequilibrium branches. Here, we take $n = 2$ as an example to demonstrate the fitting procedure. In Fig. 10a, at time $t = \tau_{01}$, the discrepancy between the master curve and the model fitting is ~350 MPa. This discrepancy can be corrected by introducing the second nonequilibrium branch with $E_2 = 350$ MPa. Based on Eq. (30) ($E(0) = E_\infty + E_1 + E_2$), one has a new E_1 equal to 1072 MPa. Assuming that the relaxation time of the second nonequilibrium branch is a decade longer than the first one, we have $\tau_{02} = 10\tau_{01}$. Following the same fitting procedure, one has moduli for the all of the five nonequilibrium branches ($E_1 = 782$ MPa, $E_2 = 350$ MPa, $E_3 = 220$ MPa, $E_4 = 50$ MPa and $E_5 = 20$ MPa).

For the shear modulus of the TSPC, $E_i = 3\bar{v}_M\mu_i$, so $\mu_1 = 555$ MPa, $\mu_2 = 248$ MPa, $\mu_3 = 156$ MPa, $\mu_4 = 36$ MPa and $\mu_5 = 14$ MPa. In Fig. 10c, the model with five nonequilibrium branches is able to precisely describe the stress relaxation master curve. Although the stress of the model relaxes faster that the experimental result at time ~10^4, the time scale is well above the practical lab time scale.

As introduced in Section 3.2.3, for temperatures above and near T_g, a_T follows the WLF equation and for temperatures below T_g, a_T follows an Arrhenius-type behavior. Fig. 10d clearly shows a_T can be characterized by these two equations, where T_r is 16 °C, C_1 is 24, C_2 is 50 °C and AF_c/k is −35,000 K.

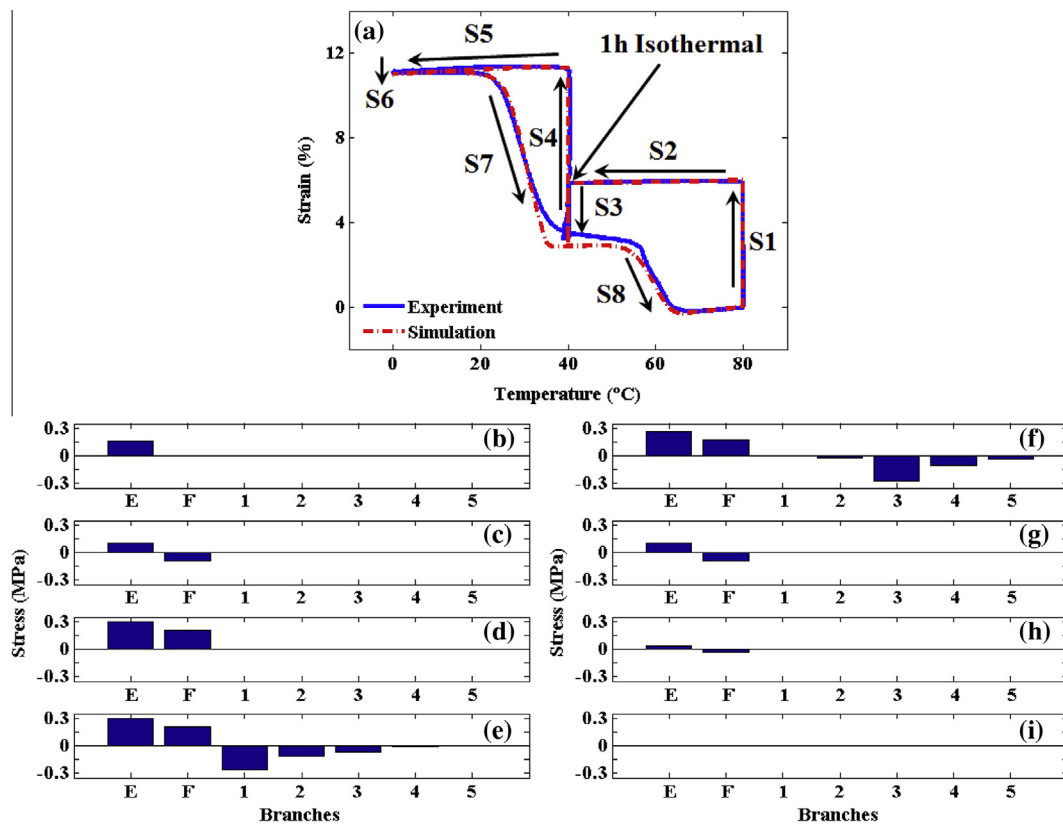### 4.2. Comparison between model simulations and experiments

The constitutive model was implemented into a user material subroutine (UMAT) in the finite element software package ABAQUS (Simulia, Providence, RI). With parameters identified by experiments listed in Table 1, the FEA simulations were performed for both dual- and triple-shape memory behaviors with the exact size of the TSPC strips under different circumstances. In simulations,

the TSPC strips were meshed by 8-node linear brick, hybrid, constant pressure, reduced integration, hourglass control elements. All degrees of freedom of the central nodes in one bottom were fixed while the remaining nodes in that bottom were modeled with rollers. The prescribed external loads were applied to the other bottom to stretch the samples.

Fig. 11a shows that the simulation successfully reproduced the experimental result of triple shape testing. The largest discrepancy occurs when unloading at 40 °C where the experimental sample fixed the first temporary shape slightly more than in the simulation. We attribute this discrepancy to the nonlinear stress–strain of the TSPC at 40 °C (in Fig. 9), which the neo-Hookean model for PCL crystals is unable to fully capture. The stress distributed across individual branches is seen in Fig. 11b–i. After loading at 80 °C (Fig. 11b), as the fiber network is in the melt state, the extension stress (0.15 MPa) is totally applied to the equilibrium branch. After unloading at 40 °C (Fig. 11c), the semicrystalline fiber network is compressed to balance the stress acting on the equilibrium branch to fix the first temporary shape. At 40 °C, the five nonequilibrium branches are inactive as the relaxation times of these branches are much shorter than the lab time scale and significant stress relaxations occur for them. Once the TSPC is stretched again with the load of 0.45 MPa at 40 °C, the extension stress is distributed to both the equilibrium branch and the fiber network (Fig. 11d). When the temperature is decreased to 0 °C, the mobility of dashpots in the five nonequilibrium branches is significantly reduced, and removing the external load at 0 °C results in the redistribution of stresses in all the branches to fix the second temporary shape. In particular, all the nonequilibrium branches are compressed to balance the extension stresses acting on the equilibrium branch and the fiber network (Fig. 11e). When heating begins, the dashpot in each nonequilibrium branch regains mobility. First, the 1st nonequilibrium branch releases its compressive stress due to its smallest relaxation time. Successively, starting from the 2nd non-

Table 1
List of material parameters.

Parameters	Value	Description
Composition		
v_M	0.82	Volume fraction of the matrix (epoxy)
v_F	0.18	Volume fraction of the fiber network (PCL)
γ_M	0.57	Stress concentration factor of the matrix (epoxy)
γ_F	2.94	Stress concentration factor of the fiber network (PCL)
Matrix		
N (m^{-3})	5.76×10^{23}	Polymer crosslinking density for the equilibrium brunch
$\mu_1, \mu_2, \mu_3, \mu_4, \mu_5$ (MPa)	555, 248, 156, 36, 14	Shear moduli for the 1st–5th nonequilibrium branches
τ_{01} (min)	3	Relaxation time for the 1st nonequilibrium branch at T_r
T_r (°C)	16	Reference temperature in WLF equation and Arrhenius-type behavior
C_1	24	WLF constant at T_r
C_2 (°C)	50	WLF constant at T_r
AF/k (K)	−35000	Pre-exponential parameter for Arrhenius-type behavior
Fiber network		
μ_C (MPa)	9.2	Shear modulus for fiber crystals (PCL)
Thermal expansion		
α_r (°C^{-1})	1.6×10^{-4}	CTE for epoxy in rubbery state
α_g (°C^{-1})	0.6×10^{-4}	CTE for epoxy in glassy state
α_m (°C^{-1})	3×10^{-4}	CTE for PCL in melted state
α_c (°G^{-1})	1.8×10^{-4}	CTE for PCL in crystallized state
V_S	2.7×10^{-2}	Volume shrink due to crystallization of PCL
Kinetics of isothermal crystallization		
k (min^{-3})	1×10^{-8}	Parameter related to the growth of the crystalline phases
n	3	Dimension of the crystalline phases

Fig. 11. (a) Shows the comparison between simulation and experiment of the triple-shape memory behavior in the strain-temperature plot; (b)–(i) show the stress distribution in individual branches during the shape memory cycle: (b) after loading at 80 °C; (c) after unloading at 40 °C; (d) after loading at 40 °C; (e) after unloading at 0 °C; (f) during heating at 25 °C; (g) during heating at 40 °C; (h) during heating at 60 °C; (i) after heating to 80 °C. The x-label "E", "F" and "1"–"5" represent the equilibrium branch, the fiber network, and the 1st–5th nonequilibrium branches.

equilibrium branch, the compressive stress first increases to maintain the overall stress equilibrium, and finally decays to zero. At 40 °C, stresses in all nonequilibrium branches are released, the

stress on the fiber network becomes compressive, and the TSPC recovers into its first temporary shape (Fig. 11g). Continued heating causes the fiber crystals commence melting, the compressive

stress on the fiber network decreases, and the TSPC starts to recover from the first temporary shape to the permanent shape (Fig. 11h). Once the fiber crystals completely melt, all stresses on all branches become zero, and the TSPC returns to its permanent shape.

Fig. 12a presents the simulation of the one-step-fixing shape memory behavior. In comparing simulation and experiment, the simulation shows good agreement. Fig. 12b–g presents the stress distribution on individual branches during the shape memory cycle. After loading at 80 °C (Fig. 12b), since the fiber network is in the melt state and all the nonequilibrium branches are inactive, the extension stress (0.2 MPa) was only applied to the equilibrium branch. After unloading at 0 °C (Fig. 12c), the stress acting on the equilibrium branch is balanced by the compressive stresses acting on the nonequilibrium branches, but no obvious compressive stress is observed acting on the fiber network, as almost 100% of the strain is fixed and the compressive strain in the fiber network is nearly zero. Once the temperature is elevated to 30 °C (Fig. 12d), as the relaxation times of all nonequilibrium branches were significantly decreased, the compressive stresses only act on the 4th and 5th nonequilibrium branches, and the semicrystalline fiber network starts to be compressed to balance certain extension stress. At 40 °C (Fig. 12e), all nonequilibrium branches turned into the inactive state and only the semicrystalline fiber network is compressed to balance the extension stress. The TSPC reaches the strain plateau from 40 to 60 °C. At 60 °C (Fig. 12f), as a part of semicrystalline fiber network melts, the compressive stress acting on the fiber network decreases and the TSPC continues the free recovery process. Once the semicrystalline fiber network completely melts, the stress stored on it is released and the TSPC recovers into its permanent shape (Fig. 12g).

4.3. Applications of the model

Having implemented our model into the user material subroutine (UMAT) in ABAQUS (Simulia, Providence, RI), it is capable to simulate complicated 3D shape memory phenomena. Here, two applications of the model, t-SMEs of a twisted sheet and a folded stick are presented.

Fig. 13 shows the t-SME of a twisted sheet. In Fig. 13a, a 5 mm × 2mm × 0.2mm sheet was meshed by 8-node linear brick, hybrid, constant pressure, reduced integration, hourglass control elements. The two surfaces parallel to the yz plane were tied to analytical rigid bodies for boundary condition definition. All degrees of freedom of one analytical rigid body were fixed to constrain one end of the sheet. At 80 °C, the other movable analytical rigid body was rotated by 90° in the counterclockwise direction to twist the sheet (Fig. 13b). The Mises stress was ∼0.1 MPa with the highest Mises stress at two corners. At 40 °C (Fig. 13d), once the boundary condition of the movable analytical rigid body was deactivated, the Mises stress throughout the sheet was reduced to zero and the sheet fixed ∼60% of the twisting (the first temporary shape), which was consistent with the t-SME in 1D manner shown in Fig. 11. Then, the analytical rigid body was rotated back to the original position at 40 °C (Fig. 13e). The high stress area with ∼0.17 MPa Mises stress was observed in the middle of the sheet. After deactivating the boundary condition of the movable analytical rigid body at 0 °C, the Mises stress throughout the sheet fell to zero again, and ∼100% of the twisting (the second temporary shape) was fixed (Fig. 13g), which was also consistent with the t-SME in 1D manner shown in Fig. 11. By heating back to 40 °C, it recovers to the first temporary shape (Fig. 13h). It returns to
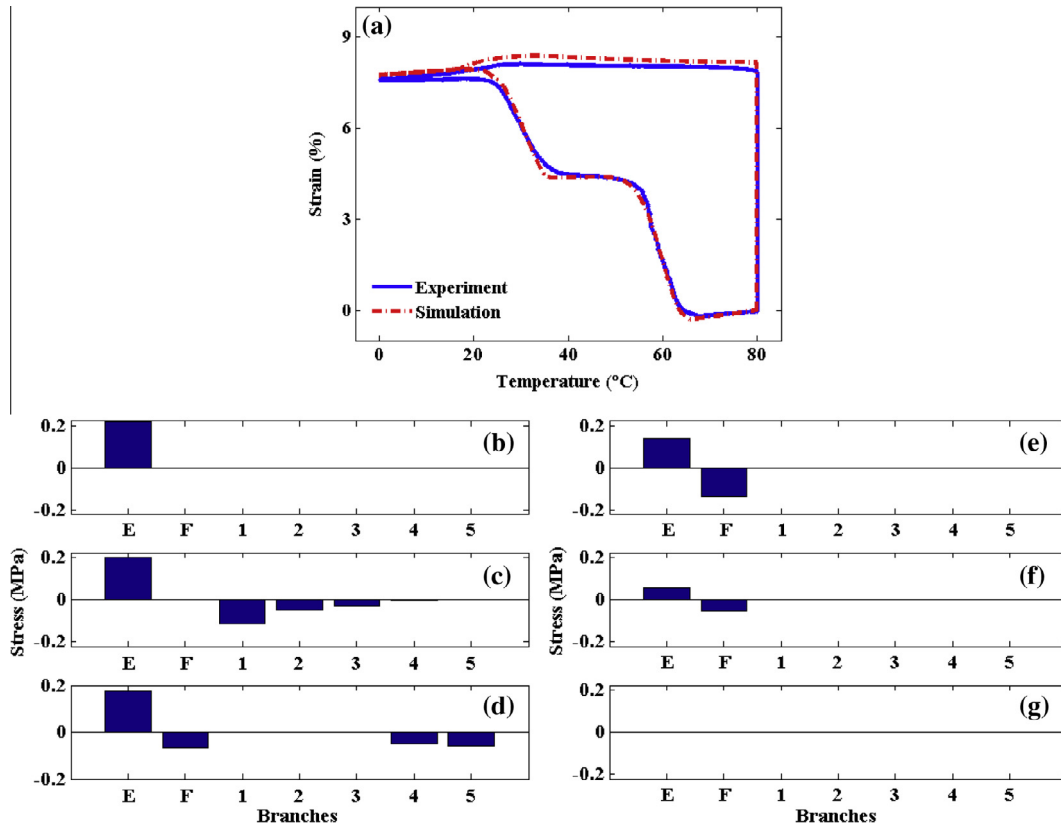

Fig. 12. (a) Shows the comparison between simulation and experiment of the one-step-fixing shape memory behavior in the strain-temperature plot; (b)–(g) show the stress distribution in individual branches during the shape memory cycle: (b) after loading at 80 °C; (c) after unloading at 0 °C; (d) during heating at 30 °C; (e) during heating at 40 °C; (f) during heating at 60 °C; (g) after heating to 80 °C. The x-label "E", "F" and "1"–"5" represent the equilibrium branch, the fiber network, and the 1st–5th nonequilibrium branches.
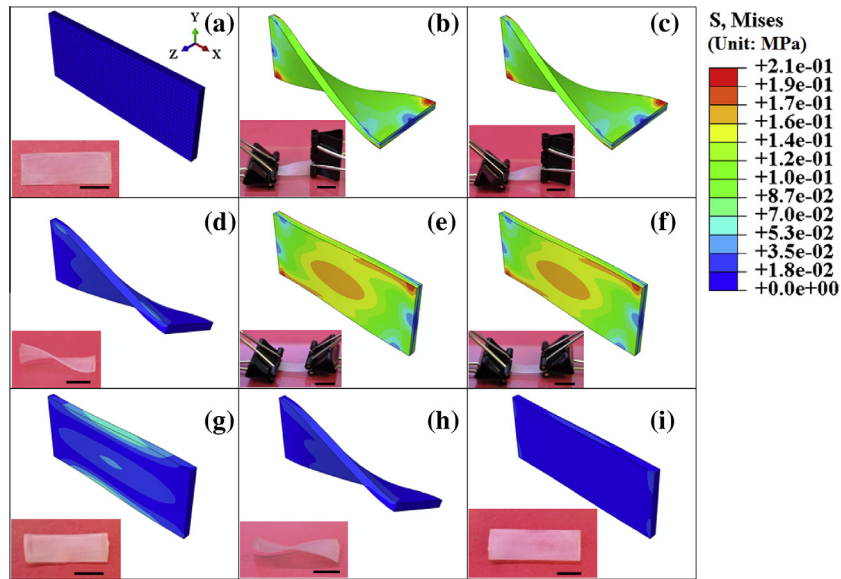
Fig. 13. Comparison between finite element simulation and experiment of a twisted sheet demonstrating t-SME: (a) initial shape; (b) after loading at 80 °C; (c) after cooling to 40 °C; (d) after unloading at 40 °C; (e) after loading at 40 °C; (f) after cooling to 0 °C; (g) after unloading at 0 °C; (h) after heating to 40 °C; (i) after heating to 80 °C. (Insets present the t-SME of the twisted sheet in experiment, and the black scale bar is 5 mm.).
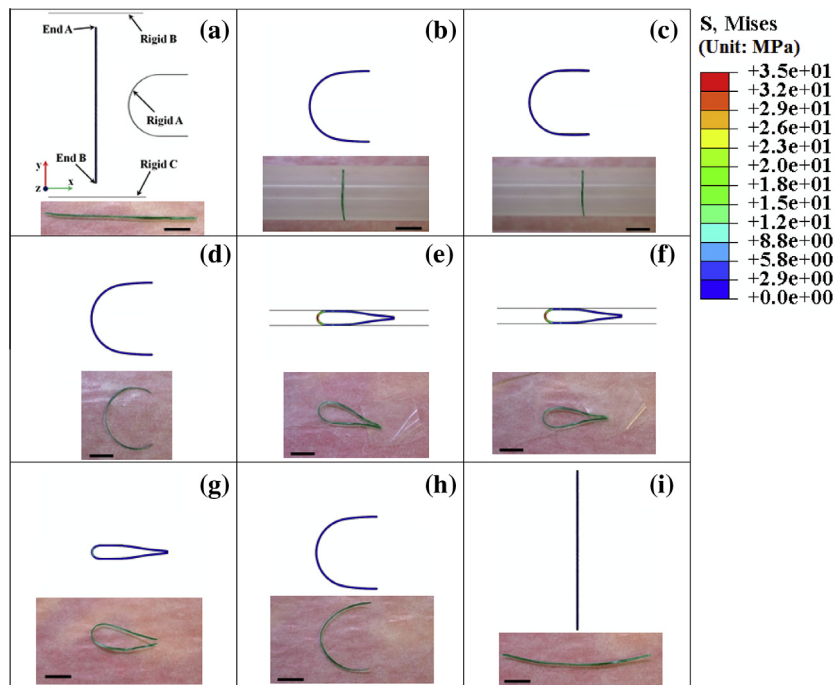
Fig. 14. Comparison between finite element simulation and experiment of a folded stick demonstrating t-SME: (a) boundary conditions; (b) after loading at 80 °C; (c) after cooling to 40 °C; (d) after unloading at 40 °C; (e) after loading at 40 °C; (f) after cooling to 0 °C; (g) after unloading at 0 °C; (h) after heating to 40 °C; (i) after heating to 80 °C. (Insets present the t-SME of the folded stick in experiment, and the black scale bar is 10 mm.).

the permanent shape at 80 °C (Fig. 13i). Insets in Figs. 13 present the real experiment of a twisted sheet exhibiting the t-SME. The experiment agrees the simulation well, which validates our model.

In Fig. 14, our model is used to simulate the t-SME of a folded stick. In Fig. 14a, a 50mm × 0.5 mm × 0.5mm sheet was meshed by 8-node linear brick, hybrid, constant pressure, reduced integration, hourglass control elements. In Fig. 14a, both End A and End B were constrained in the x-direction. In order to prevent the stick from rigid motion, one surface parallel to the xy plane was constrained in the z-direction. At 80 °C, Rigid A moved in the negative

x-direction to deform the stick into a "C" shape (Fig. 14b). At 40 °C (Fig. 14d), once Rigid A was removed, the Mises stress throughout the stick was reduced to zero, and the stick stayed at the "C" shape (the first temporary shape). Then, after being compressed by Rigid B and Rigid C, the "C" stick was folded (Fig. 14e). At 0 °C (Fig. 14d); when the Rigid B and Rigid C were removed, the Mises stress throughout the stick was reduced to zero, and the stick stayed at the folded shape (the second temporary shape). During heating, the ring transformed from the folded shape to the "C" shape (the first temporary shape) at 40 °C (Fig. 14h), and eventually returned

to the shape original at 80 °C (Fig. 14i). Insets in Fig. 14 present the real experiment of a folded stick exhibiting the t-SME. The results of the experiment show slightly different from those of the simulation primarily due to the slightly different of the tools inducing deformation. Overall, the simulation agrees the experiment well.

5. Conclusion

Triple-shape memory behaviors of a TSPC were investigated in this paper using a full 3D model. In the TSPC system, an amorphous SMP (epoxy) serves as a matrix to fix one temporary shape and a crystallizable fiber network (PCL) is utilized to fix the other temporary shape. During heating, the material sequentially recovers from the second temporary shape to the first one and eventually its permanent shape. A 3D finite deformation thermomechanical constitutive model was introduced to capture t-SMEs of the TSPC. In this model, a multi-branch approach was used to describe viscoelastic behavior of the amorphous SMP matrix, and the constitutive model with differently deformed crystalline phases was used to describe the SM behaviors of crystallizable fiber networks. Experimental results including uniaxial tensions, thermal expansions, and stress relaxation tests were used to identify parameters in the model. Using the implemented user material subroutine (UMAT), the constitutive model successfully reproduced different types of shape memory behaviors exhibited in experiments, including dual-shape memory behaviors under different temperature ranges, the one-step-fixing shape memory behavior and the triple-shape memory behavior. Stress distribution analyses were also performed to visualize the stress distribution during those different shape memory behaviors. The model was also able to simulate complicated triple shape phenomena, such as a twisted sheet and a folded stick demonstrating t-SME, inspiring future experiments.

Acknowledgments

References

Ames, N.M., Srivastava, V., Chester, S.A., Arland, L., 2009. A thermo-mechanically coupled theory for large deformations of amorphous polymers. Part II: applications. Int. J. Plast. 25, 1495–1539.

Anand, L., Ames, N.M., Srivastava, V., Chester, S.A., 2009. A thermo-mechanically coupled theory for large deformations of amorphous polymers. Part I: formulation. Int. J. Plast. 25, 1474–1494.

Arruda, E.M., Boyce, M.C., 1993. A three-dimensional constitutive model for the large stretch behavior of rubber elastic materials. J. Mech. Phys. Solids 41, 389–412.

Avrami, M., 1939. Kinetics of phase change I – general theory. J. Chem. Phys. 7, 1103–1112.

Avrami, M., 1940. Kinetics of phase change II – transformation-time relations for random distribution of nuclei. J. Chem. Phys. 8, 212–224.

Avrami, M., 1941. Granulation, phase change, and microstructure – kinetics of phase change. III. J. Chem. Phys. 9, 177–184.

Barot, G., Rao, I.J., 2006. Constitutive modeling of the mechanics associated with crystallizable shape memory polymers. Z. Angew. Math. Phys. 57, 652–681.

Bellin, I., Kelch, S., Langer, R., Lendlein, A., 2006. Polymeric triple-shape materials. Proc. Nat. Acad. Sci. USA 103, 18043–18047.

Bellin, I., Kelch, S., Lendlein, A., 2007. Dual-shape properties of triple-shape polymer networks with crystallizable network segments and grafted side chains. J. Mater. Chem. 17, 2885–2891.

Benveniste, Y., 1987. A new approach to the application of Mori–Tanaka theory in composite-materials. Mech. Mater. 6, 147–157.

Boyce, M.C., Parks, D.M., Argon, A.S., 1988. Computational modeling of large strain plastic-deformation in glassy-polymers. Abstract Pap. Am. Chem. Soc. 196, 156-POLY.

Castaneda, P.P., 1991. The effective mechanical-properties of nonlinear isotropic composites. J. Mech. Phys. Solids 39, 45–71.

Davis, K.A., Burke, K.A., Mather, P.T., Henderson, J.H., 2011. Dynamic cell behavior on shape memory polymer substrates. Biomaterials 32, 2285–2293.

Diani, J., Liu, Y.P., Gall, K., 2006. Finite strain 3D thermoviscoelastic constitutive model for shape memory polymers. Polym. Eng. Sci. 46, 486–492.

Dunn, M.L., 1997. One-dimensional composite micromechanics. Int. J. Mech. Eng. Educ. 26, 38–50.

Ferry, J.D., 1980. Viscoelastic Properties of Polymers, third ed. Wiley, New York.

Flory, P.J., 1953. Principles of Polymer Chemistry. Cornell University Press, Ithaca.

Ge, Q., Luo, X.F., Rodriguez, E.D., Zhang, X., Mather, P.T., Dunn, M.L., Qi, H.J., 2012. Thermomechanical behavior of shape memory elastomeric composites. J. Mech. Phys. Solids 60, 67–83.

Ge, Q., Luo, X.F., Iverson, C.B., Mather, P.T., Dunn, M.L., Qi, H.J., 2013. Mechanisms of triple-shape polymeric composites due to dual thermal transitions. Soft Matter 7, 2212–2223.

Gent, A.N., 1996. A new constitutive relation for rubber. Rubber Chem. Technol. 69, 59–61.

Hermiller, J., Ahn, D.U., Castro, F., Westbrook, K.K., Ding, Y.F., Qi, H.J., 2011. Time and temperature dependent recovery of epoxy-based shape memory polymers. J. Eng. Mater. -T. ASME 133, 021025.

Huang, W.M., Yang, B., An, L., Li, C., Chan, Y.S., 2005. Water-driven programmable polyurethane shape memory polymer: demonstration and mechanism. Appl. Phys. Lett. 86, 114105.

Hutchinson, J.M., 1995. Physical aging of polymers. Prog. Polym. Sci. 20, 703–760.

Jiang, H.Y., Kelch, S., Lendlein, A., 2006. Polymers move in response to light. Adv. Mater. 18, 1471–1475.

Koerner, H., Price, G., Pearce, N.A., Alexander, M., Vaia, R.A., 2004. Remotely actuated polymer nanocomposites – stress-recovery of carbon-nanotube-filled thermoplastic elastomers. Nat. Mater. 3, 115–120.

Kovacs, A.J., Aklonis, J.J., Hutchinson, J.M., Ramos, A.R., 1979. Isobaric volume and enthalpy recovery of glasses. 2. Transparent multi-parameter theory. J. Polym. Sci. Polym. Phys. 17, 1097–1162.

Lendlein, A., Kelch, S., 2002. Shape-memory polymers. Angew. Chem. Int. Ed. Engl. 41, 2035–2057.

Lendlein, A., Kelch, S., 2005. Shape-memory polymers as stimuli-sensitive implant materials. Clin. Hemorheol. Microcirculation 32, 105–116.

Lendlein, A., Jiang, H.Y., Junger, O., Langer, R., 2005. Light-induced shape-memory polymers. Nature 434, 879–882.

Li, M.H., Keller, P., Li, B., Wang, X.G., Brunet, M., 2003. Light-driven side-on nematic elastomer actuators. Adv. Mater. 15, 569–572.

Liu, Y.P., Gall, K., Dunn, M.L., McCluskey, P., 2004. Thermomechanics of shape memory polymer nanocomposites. Mech. Mater. 36, 929–940.

Liu, Y.P., Gall, K., Dunn, M.L., Greenberg, A.R., Diani, J., 2006. Thermomechanics of shape memory polymers: uniaxial experiments and constitutive modeling. Int. J. Plast. 22, 279–313.

Liu, C., Qin, H., Mather, P.T., 2007. Review of progress in shape-memory polymers. J. Mater. Chem. 17, 1543–1558.

Long, K.N., Scott, T.F., Qi, H.J., Bowman, C.N., Dunn, M.L., 2009. Photomechanics of light-activated polymers. J. Mech. Phys. Solids 57, 1103–1121.

Long, K.N., Dunn, M.L., Qi, H.J., 2010a. Mechanics of soft active materials with phase evolution. Int. J. Plast. 26, 603–616.

Long, K.N., Dunn, M.L., Scott, T.F., Turpin, L.P., Qi, H.J., 2010b. Light-induced stress relief to improve flaw tolerance in network polymers. J. Appl. Phys. 107, 053519.

Long, K.N., Scott, T.F., Dunn, M.L., Qi, H.J., 2011. Photo-induced deformation of active polymer films: single spot irradiation. Int. J. Solids Struct. 48, 2089–2101.

Long, R., Qi, H.J., Dunn, M.L., 2013. Thermodynamics and mechanics of photochemcially reacting polymers. J. Mech. Phys. Solids 61, 2212–2239.

Luo, X.F., Mather, P.T., 2009. Preparation and characterization of shape memory elastomeric composites. Macromolecules 42, 7251–7253.

Luo, X.F., Mather, P.T., 2010. Triple-shape polymeric composites (TSPCs). Adv. Funct. Mater. 20, 2649–2656.

Mather, P.T., Luo, X.F., Rousseau, I.A., 2009. Shape memory polymer research. Annu. Rev. Mater. Res. 39, 445–471.

McKenna, G.B., 1989. Glass formation and glassy behavior. In: Booth, C., Price, C. (Eds.), Comprehensive Polymer Science. Pergamon Press, Oxford, pp. 311–362.

Mohr, R., Kratz, K., Weigel, T., Lucka-Gabor, M., Moneke, M., Lendlein, A., 2006. Initiation of shape-memory effect by inductive heating of magnetic nanoparticles in thermoplastic polymers. Proc. Natl. Acad. Sci. USA 103, 3540–3545.

Mooney, M., 1940. A theory of large elastic deformation. J. Appl. Phys. 11, 582–592.

Moynihan, C.T., Easteal, A.J., Debolt, M.A., Tucker, J., 1976. Dependence of fictive temperature of glass on cooling rate. J. Am. Ceram. Soc. 59, 12–16.

Nguyen, T.D., Qi, H.J., Castro, F., Long, K.N., 2008. A thermoviscoelastic model for amorphous shape memory polymers: incorporating structural and stress relaxation. J. Mech. Phys. Solids 56, 2792–2814.

O'Connell, P.A., McKenna, G.B., 1999. Arrhenius-type temperature dependence of the segmental relaxation below T-g. J. Chem. Phys. 110, 11054–11060.

Ozawa, T., 1971. Kinetics of non-isothermal crystallization. Polymer 12, 150-&.

Qi, H.J., Nguyen, T.D., Castro, F., Yakacki, C.M., Shandas, R., 2008. Finite deformation thermo-mechanical behavior of thermally induced shape memory polymers. J. Mech. Phys. Solids 56, 1730–1751.

Rajagopal, K.R., Srinivasa, A.R., 1998a. Mechanics of the inelastic behavior of materials – Part 1, theoretical underpinnings. Int. J. Plast. 14, 945–967.

Rajagopal, K.R., Srinivasa, A.R., 1998b. Mechanics of the inelastic behavior of materials. Part II: inelastic response. Int. J. Plast. 14, 969–995.

Rivlin, R.S., 1948. Large elastic deformations of isotropic materials. IV. Further developments of the general theory. Philos. Trans. R. Soc. London. Ser. A Math. Phys. Sci. 241, 379–397.

Robertson, R.E., Simha, R., Curro, J.G., 1984. Free-volume and the kinetics of aging of polymer glasses. Macromolecules 17, 911–919.

Ryu, J., D'Amato, M., Cui, X.D., Long, K.N., Qi, H.J., Dunn, M.L., 2012. Photo-origami-bending and folding polymers with light. Appl. Phys. Lett. 100, 161908.

Scott, T.F., Schneider, A.D., Cook, W.D., Bowman, C.N., 2005. Photoinduced plasticity in cross-linked polymers. Science 308, 1615–1617.

Scott, T.F., Draughon, R.B., Bowman, C.N., 2006. Actuation in crosslinked polymers via photoinduced stress relaxation. Adv. Mater. 18, 2128–2132.

Srivastava, V., Chester, S.A., Ames, N.M., Anand, L., 2010a. A thermo-mechanically-coupled large-deformation theory for amorphous polymers in a temperature range which spans their glass transition. Int. J. Plast. 26, 1138–1182.

Srivastava, V., Chester, S.A., Anand, L., 2010b. Thermally actuated shape-memory polymers: experiments, theory, and numerical simulations. J. Mech. Phys. Solids 58, 1100–1124.

Tobushi, H., Hara, H., Yamada, E., Hayashi, S., 1996a. Thermomechanical properties in a thin film of shape memory polymer of polyurethane series. Smart Mater. Struct. 5, 483–491.

Tobushi, H., Hayashi, S., Ikai, A., Hara, H., 1996b. Thermomechanical properties of shape memory polymers of polyurethane series and their applications. J. Phys. Iv 6, 377–384.

Wang, Z., Hansen, C., Ge, Q., Maruf, S.H., Ahn, D.U., Qi, H.J., Ding, Y.F., 2011. Programmable, pattern-memorizing polymer surface. Adv. Mater. 23, 3669-+.

Westbrook, K.K., Castro, F., Long, K.N., Slifka, A.J., Qi, H.J., 2010a. Improved testing system for thermomechanical experiments on polymers using uniaxial compression equipment. Polym. Testing 29, 503–512.

Westbrook, K.K., Parakh, V., Chung, T., Mather, P.T., Wan, L.C., Dunn, M.L., Qi, H.J., 2010b. Constitutive modeling of shape memory effects in semicrystalline polymers with stretch induced crystallization. J. Eng. Mater.-T. ASME 132, 041010.041011-041019.

Westbrook, K.K., Kao, P.H., Castro, F., Ding, Y.F., Qi, H.J., 2011a. A 3D finite deformation constitutive model for amorphous shape memory polymers: a multi-branch modeling approach for nonequilibrium relaxation processes. Mech. Mater. 43, 853–869.

Westbrook, K.K., Mather, P.T., Parakh, V., Dunn, M.L., Ge, Q., Lee, B.M., Qi, H.J., 2011b. Two-way reversible shape memory effects in a free-standing polymer composite. Smart Mater. Struct. 20.

Xie, T., 2010. Tunable polymer multi-shape memory effect. Nature 464, 267–270.

Xie, T., 2011. Recent advances in polymer shape memory. Polymer 52, 4985–5000.

Xie, T., Xiao, X.C., Cheng, Y.T., 2009. Revealing triple-shape memory effect by polymer bilayers. Macromol. Rapid Commun. 30, 1823–1827.

Yakacki, C.M., Shandas, R., Lanning, C., Rech, B., Eckstein, A., Gall, K., 2007. Unconstrained recovery characterization of shape-memory polymer networks for cardiovascular applications. Biomaterials 28, 2255–2263.